IVYSPRING INTERNATIONAL PUBLISHER

*Theranostics*

2018; 8(7): 1782-1797. doi: 10.7150/thno.22621

Research Paper

# Dual-Energy CT Imaging of Tumor Liposome Delivery After Gold Nanoparticle-Augmented Radiation Therapy

Jeffrey R. Ashton[1,2], Katherine D. Castle[3], Yi Qi[1], David G. Kirsch[3,4], Jennifer L. West[2], Cristian T. Badea[1,2]✉

1. Center for In Vivo Microscopy, Department of Radiology, Duke University Medical Center, Durham, NC 27710, United States
2. Department of Biomedical Engineering, Duke University, Durham, NC, 27705, United States
3. Department of Pharmacology and Cancer Biology, Duke University, Durham, NC, 27705, United States
4. Department of Radiation Oncology, Duke University Medical Center, Durham, NC, 27710, United States

✉ Corresponding author: cristian.badea@duke.edu



Received: 2017.08.31; Accepted: 2018.01.22; Published: 2018.02.12

## Abstract

Gold nanoparticles (AuNPs) are emerging as promising agents for both cancer therapy and computed tomography (CT) imaging. AuNPs absorb x-rays and subsequently release low-energy, short-range photoelectrons during external beam radiation therapy (RT), increasing the local radiation dose. When AuNPs are near tumor vasculature, the additional radiation dose can lead to increased vascular permeability. This work focuses on understanding how tumor vascular permeability is influenced by AuNP-augmented RT, and how this effect can be used to improve the delivery of nanoparticle chemotherapeutics.

**Methods:** Dual-energy CT was used to quantify the accumulation of both liposomal iodine and AuNPs in tumors following AuNP-augmented RT in a mouse model of primary soft tissue sarcoma. Mice were injected with non-targeted AuNPs, RGD-functionalized AuNPs (vascular targeting), or no AuNPs, after which they were treated with varying doses of RT. The mice were injected with either liposomal iodine (for the imaging study) or liposomal doxorubicin (for the treatment study) 24 hours after RT. Increased tumor liposome accumulation was assessed by dual-energy CT (iodine) or by tracking tumor treatment response (doxorubicin).

**Results:** A significant increase in vascular permeability was observed for all groups after 20 Gy RT, for the targeted and non-targeted AuNP groups after 10 Gy RT, and for the vascular-targeted AuNP group after 5 Gy RT. Combining targeted AuNPs with 5 Gy RT and liposomal doxorubicin led to a significant tumor growth delay (tumor doubling time ~ 8 days) compared to AuNP-augmented RT or chemotherapy alone (tumor doubling time ~3-4 days).

**Conclusions:** The addition of vascular-targeted AuNPs significantly improved the treatment effect of liposomal doxorubicin after RT, consistent with the increased liposome accumulation observed in tumors in the imaging study. Using this approach with a liposomal drug delivery system can increase specific tumor delivery of chemotherapeutics, which has the potential to significantly improve tumor response and reduce the side effects of both RT and chemotherapy.

Key words: dual-energy CT, radiation therapy, nanoparticles, tumor drug delivery, vascular imaging, small animal imaging

## Introduction

Radiation therapy (RT) is one of the most commonly used treatments for cancer, either as monotherapy or in conjunction with surgery and/or chemotherapy. X-ray RT can cause direct ionization of DNA within target cells as well as the ionization of water, producing free radicals, which cause additional indirect DNA damage. DNA damage can lead to cellular arrest or cell death, making RT an effective

treatment for cancer. However, radiation can also affect healthy tissues, and if normal tissue dose tolerances are exceeded, serious complications in tissues surrounding the treated tumor may arise [1-3]. Therefore, one of the main challenges in RT is to increase the therapeutic index, either by increasing the effectiveness of the radiation within the target tissue (thereby reducing the necessary dose) or by reducing the damage caused by the radiation in the surrounding normal tissues [4].

Gold nanoparticles (AuNPs) have been shown to be a promising RT enhancer [5]. Because AuNPs have a high atomic number, they strongly absorb low and medium-energy x-rays (~10-250 keV) via the photoelectric effect. When the photoelectric effect occurs, a secondary electron is ejected from the gold atom as well as a characteristic x-ray or Auger electrons. These pass out of the nanoparticle surface into the surrounding environment and can cause additional local damage. The secondary electrons have a very short range (>99% deposited within 250 nm), so most of the extra energy deposition affects cells that are in direct proximity to the nanoparticles, thereby increasing their radiation dose [6]. Because appropriately-sized gold nanoparticles can selectively accumulate in tumors either passively due to the enhanced permeability and retention (EPR) effect [7, 8] or actively via targeting, they have the potential to be very effective in tumor RT augmentation without increasing the dose to surrounding normal tissues. AuNPs have also frequently been used as contrast agents for x-ray computed tomography (CT) imaging [9-14] due to their strong x-ray absorbance, making them excellent agents for combined treatment and imaging.

Gold nanoparticles have been used to augment RT in several prior studies [5, 14-21]. Hainfeld et al. have shown that tumors loaded with AuNPs respond better to RT. In a mouse model of malignant glioma, the one-year survival was 86% with AuNP-augmented RT versus 20% with RT alone and 0% with AuNPs alone [17]. Monte Carlo simulations and biological studies have estimated that the radiation dose enhancement due to gold nanoparticles can vary from 10% up to 500% for orthovoltage x-rays, depending on the nanoparticle size, concentration, and other experimental parameters [22-25]. A majority of studies, however, demonstrate a radiation dose enhancement of between 40% and 80% in the presence of gold nanoparticles [26]. Some of the most important factors determining the dose enhancement identified in these studies include the gold nanoparticle concentration and the mean energy of the x-ray beam. Because the x-ray interactions with gold are predominately due to the photoelectric effect, the highest absorption occurs with x-rays that are close to the k-edge of gold (80.7 keV).

The distribution of nanoparticles within a tissue is also an important factor in radiation dose enhancement. After nanoparticles are injected intravenously and pass through the endothelial fenestra into a tumor, their fate depends on nanoparticle size. Very small nanoparticles (< 10 nm diameter) can diffuse through the tumor tissue and distribute relatively homogeneously in most cases. Diffusion of larger nanoparticles through tumor tissue is more limited, so they initially remain near the blood vessels and then slowly diffuse away over time [27]. A homogeneous distribution of dose enhancement through the tumor is ideal for tumor treatment, so smaller nanoparticles are generally preferred. With larger nanoparticles, there is an uneven distribution of dose enhancement in the tumor, which is primarily focused around the tumor blood vessels. However, a higher concentration of gold near the vasculature could provide a biological advantage over a homogeneous distribution for some applications. A higher radiation dose to the endothelium could increase vascular permeability, which can improve tumor delivery of chemotherapeutic drugs. This strategy could even lead to complete tumor vascular disruption, prompting extensive tumor cell death [6]. The effect on tumor vasculature can be further increased if the gold nanoparticles are directly attached to the endothelial cells by targeting ligands. Monte Carlo simulations have estimated that the effect of radiation on endothelial cells would be increased by ~43% compared to RT alone when gold nanoparticles are located in or around the blood vessels, but up to 200% when the nanoparticles are directly attached to the endothelial wall [28]. A study examining the effect of endothelial-targeted gold nanoparticles in RT has shown significant disruption of vascular structures on microscopic exam, including altered vessel morphology, endothelial cell detachment, and disruption of the basement membrane. These vascular changes were not seen in tumors treated with RT in the absence of the gold nanoparticles [29].

One of the most commonly used ligands for targeting tumor epithelium is the RGD (Arg-Gly-Asp) peptide, which has high affinity for the transmembrane heterodimer $\alpha_v\beta_3$ integrin receptor [30, 31]. The $\alpha_v\beta_3$ integrin receptor is strongly involved in the regulation of angiogenesis and is present on activated endothelial cells in the neovasculature within tumors. Cyclization of the RGD peptide is commonly used to improve the binding properties of the peptide by conferring rigidity to the structure,

which increases the potency and specificity of the peptide for the $\alpha_v\beta_3$ integrin target and reduces the susceptibility of the peptide to degradation [30]. These targeting ligands can be readily conjugated to the surface of gold nanoparticles via gold-thiol bonds [29, 32], producing vascular-targeted gold nanoparticles.

The goal of this study was to quantify the effect of both non-targeted and vascular-targeted gold nanoparticles on RT-induced tumor vascular disruption in a mouse model of primary soft tissue sarcoma and then to exploit those effects to increase tumor delivery of liposomal chemotherapeutics. Liposomal chemotherapy has the potential to improve the efficacy of cancer treatment by increasing the dose delivered to the tumor while reducing the required systemic dose and the associated side effects. However, the effectiveness of liposomal agents depends primarily on the EPR effect [7, 33]. In humans, the EPR effect is highly variable due to significant heterogeneity in tumor vascular permeability. Increasing tumor vascular permeability could significantly improve delivery of liposomal chemotherapy. We have previously used dual-energy CT imaging to measure increased vascular permeability in mouse primary soft tissue sarcomas [34] after RT as well as in the heart in a model of radiation-induced cardiac injury [35]. In these studies, nanoparticle contrast agents (either liposomal iodine or gold nanoparticles) were injected intravenously into mice after irradiation. Vascular permeability was assessed by measuring the accumulation of gold or iodine nanoparticles within the tissue by dual-energy CT. In both cases, the accumulation of nanoparticles increased significantly after RT.

In this study, we assessed the effect of AuNP-augmented RT on tumor vascular permeability using dual-energy CT imaging of liposomal iodine. Dual-energy CT is an advanced imaging technique that allows for selective visualization and quantification of multiple high atomic weight materials in a single scan. Liposomal iodine uptake in soft tissue sarcomas was quantified after irradiation with different radiation doses (0 Gy, 5 Gy, 10 Gy, or 20 Gy) augmented with vascular-targeted AuNPs, non-targeted AuNPs, or no AuNPs. For each group, a dual-energy decomposition was performed to separate the gold and iodine CT signals and quantify each independently. We measured the accumulation of liposomal iodine in the tumors following irradiation to evaluate tumor vascular permeability. We compared the radiation dose and type of AuNPs (vascular-targeted vs. non-targeted) to maximize the tumor vascular permeability to liposomes. The liposomal iodine accumulation in each of these cases acted as an easily-quantified surrogate for the liposomal chemotherapy accumulation that would occur under similar conditions. We then used the optimal conditions from the imaging study to demonstrate improved therapeutic efficacy of liposomal chemotherapy following AuNP-augmented RT. Our approach could be employed to enhance the delivery of chemotherapy into tumors, while respecting maximally tolerated drug levels for normal tissues. Combining RT, AuNPs, and chemotherapy may improve patient outcomes more than RT or chemotherapy alone or in combination with each other. Moreover, by combining RT, AuNPs, and chemotherapy it may be possible to achieve an equivalent tumor response using a smaller dose of RT and/or chemotherapy, thereby minimizing normal tissue injury.

## Materials and Methods

### Gold Nanoparticle Synthesis

Gold nanoparticles (~25 nm) were synthesized via the citrate reduction of gold chloride salt using a modified Frens method [36]. 50.55 mL of $HAuCl_4$ (10 mg/mL) was added to 1.5 L of ultrapure water and the solution was brought to boiling. 9 mL of sodium citrate solution (100 mg/mL) was rapidly injected into the gold solution under vigorous mixing, after which the solution quickly changed color from yellow to deep red. The solution was maintained at 100°C and mixed for an additional 15 minutes to complete the reaction, and then the solution was cooled to room temperature. The nanoparticles were then passed through a 0.22 μm filter to remove any aggregates that may have formed during the reaction. The size and polydispersity of the nanoparticles were determined by transmission electron microscopy (TEM) using an FEI Tecnai G² Twin TEM operated at 200 mV (FEI Company, Hillsboro, OR).

### Liposomal Iodine Synthesis

Liposomal iodine was synthesized as described previously [37]. A lipid mixture (200 mmol/L) consisting of 1,2-dipalmitoyl-sn-glycero-3-phosphocholine (DPPC), cholesterol, and 1,2-distearoyl-sn-glycero-3-phosphoethanolamine-N-[methoxy(polyethylene glycol)-2000] (DSPE-MPEG 2000) in a 55:40:5 molar ratio was dissolved in 1 mL ethanol and then hydrated with 9 mL of a concentrated iodixanol solution (550 mg iodine/mL). The resulting lipid solution was sequentially extruded on a Lipex Thermoline extruder (Northern Lipids, Vancouver, British Columbia, Canada) to size the liposomes to ~120 nm. The liposome solution was diafiltered using a MicroKros® module (Spectrum Laboratories, CA) to remove un-encapsulated iodixanol and ethanol and to suspend the liposome in phosphate-buffered saline

(PBS, pH 7.4). The resultant liposomes were kept at 4°C until ready for use. The size distribution of liposomes in the final formulation was determined by dynamic light scattering (DLS) using a Malvern Zetasizer Nanoseries (Malvern Instruments, Worcestershire, UK) at 25°C.

### Targeted Nanoparticle Synthesis

Vascular-targeted nanoparticles were formed by linking cyclic RGD peptides (c(RGDfK), Anaspec) to the nanoparticle surface. The RGD peptides were attached to the gold nanoparticles via a 5 kDa heterobifunctional poly(ethylene glycol) (PEG) linker molecule, orthopyridyl disulfide PEG succinimidyl valerate (OPSS-PEG-SVA, Laysan Bio). The peptides were PEGylated by reacting the OPSS-PEG-SVA with the RGD at a ratio of 3:1 (PEG:peptide) in HEPES-buffered saline at pH 8.6 at 4°C overnight. Unconjugated peptides were removed via dialysis in ultrapure water using a 1 kDa MWCO regenerated cellulose membrane. OPSS-PEG-RGD was then reacted with tris(2-carboxyethyl) phosphine (TCEP) for 30 minutes to reduce the OPSS disulfide into free thiols. This mixture was then added directly to a solution of bare AuNPs (1:8 ratio of PEG:AuNP by mass). These nanoparticles were rocked at room temperature for 2 hours, after which 5 kDa PEG-SH was added (1:4 PEG:AuNP by mass) to passivate the remaining gold surface. After rocking overnight, 5 kDa PEG-SH was again added to fully passivate the AuNP surface (1:2 mass ratio). Non-targeted AuNPs (PEG-AuNPs) were also produced by adding a large excess of PEG-SH (5 kDa) to bare gold nanoparticles in the absence of the RGD peptide. All gold nanoparticles were rocked overnight at 4°C after PEG addition and then rinsed by centrifugation. The nanoparticles were sterilized via filtration (0.22 μm) and concentrated by centrifugal filtration at 1,500 x g using Amicon Ultra 15 mL 30 kDa MWCO filters (MilliporeSigma, Burlington, MA) prior to use. Hydrodynamic diameter and zeta potential of the nanoparticles were determined using a Malvern Zetasizer Nanoseries at 25°C.

### In Vitro Targeting Study

To verify effective binding of RGD-AuNPs to endothelial cells, a targeting study was performed in vitro with human umbilical vein endothelial cells (HUVECs). HUVECs (Lonza, Walkersville, MD) were grown in endothelial growth medium (EGM-2, Lonza), supplemented with vascular endothelial growth factor (VEGF), fibroblast growth factor basic (hFGFb), ascorbic acid, hydrocortisone, insulin-like growth factor-1, gentamicin, amphotericin-B, and 2% fetal bovine serum (EGM-2 BulletKit, Lonza). HUVECs were cultured in 4-well chamber slides until they reached ~90% confluence. AuNPs were then added to the media (PEG-AuNPs or RGD-AuNPs) at a concentration of 1 mg Au/mL or 6 mg Au/mL. The cells were incubated with AuNPs overnight, after which the AuNP-containing media was removed by aspiration and the cells were rinsed two times with fresh media and two times with PBS. The cells were then fixed with 4% paraformaldehyde and imaged using darkfield microscopy to visualize the gold nanoparticles associated with the cells. Darkfield microscopy was performed using a Zeiss Axiovert 135 inverted microscope (Carl Zeiss Inc., Thornwood, NY) and a Cytoviva darkfield condenser (Cytoviva, AL). All images were acquired using a 20x objective lens. With darkfield imaging, indirect sample illumination enables image production from light scattered by the samples. Gold nanoparticles are readily detected due to their increased scattering properties relative to the surrounding cells [38].

### In Vivo Nanoparticle Biodistribution Study

All animal studies were performed in accordance with protocols approved by the Duke University Institutional Animal Care and Use Committee. For determining in vivo nanoparticle kinetics and biodistribution, C57BL/6 mice (n=3 in each group) were injected by tail vein with PEG-AuNPs or RGD-AuNPs (160 mg Au/mL in PBS, 0.125 mL). Dual-energy CT imaging was performed at 0, 4, 24, and 48 hours post-injection to track the gold nanoparticle concentration in the vasculature. Gold nanoparticle concentrations within the blood were calculated at each time point using dual-energy decomposition, as described below. The approximate blood half-life for the PEG-AuNPs and RGD-AuNPs was calculated by fitting the measured concentrations to an exponential decay equation. Gold nanoparticle concentrations in the liver and spleen at 48 hours were also calculated using the dual-energy CT results as described below.

### Sarcoma Irradiation

Primary sarcomas were generated by hindlimb intramuscular injection of an adenovirus expressing Cre recombinase into LSL-Kras$^{G12D}$; p53$^{FL/FL}$ conditional mutant mice [39]. Because Cre is not expressed in the tumor vasculature of these mice, all the mice in this study have wild-type vasculature. Tumors developed 2-3 months after injection. Tumors were treated with irradiation after they reached a tumor volume of approximately 70-200 mm$^3$.

The sarcomas were irradiated with parallel-opposed anterior and posterior fields using the X-RAD 225Cx small animal image-guided irradiator

(Precision X-Ray, Inc.). The tumor was localized to isocenter via fluoroscopy at 40 kVp, 2.5 mA using a 2 mm Al filter. Irradiation was performed with an x-ray beam at 225 kVp and 13 mA and a 0.3 mm Cu filter. A square collimator was used to produce a 40 mm x 40 mm radiation field at isocenter. The RT dose was controlled by irradiation time, with an average dose rate of 300 cGy/min [34]. The mean x-ray energy of this system at 225 kVp is approximately 86.9 keV, which is just above the k-edge of gold (80.7 keV). This close concordance of gold k-edge and x-ray energy should maximize the x-ray absorption of the gold nanoparticles by the photoelectric effect.

## Dual-Energy Imaging of Vascular Permeability

A total of 55 mice with primary sarcomas were randomized into 9 different groups for the imaging study, as shown in Table 1. The treated mice were injected with PEG-AuNPs, RGD-AuNPs or no AuNPs prior to RT. 24 hours prior to irradiation, gold nanoparticles were injected IV by tail vein injection (0.125 mL, 160 mg Au/mL in PBS). The mouse hindlimbs were then irradiated with a dose of 5 Gy, 10 Gy, 20 Gy or no radiation. The mice were injected with liposomal iodine (0.3 mL, 120 mg iodine/mL in PBS) 24 hours after RT, at which point radiation causes significant endothelial cell death in this model [40, 41]. Dual-energy CT imaging was performed three days after liposomal iodine injection in order to quantify the amount of iodine accumulated within each of the tumors. The study protocol is illustrated in Figure 1. At the conclusion of dual-energy CT imaging, the mice were euthanized and tumors were harvested.

## Dual-Energy Micro-CT

All CT imaging was performed using a dual-source micro-CT system developed in-house [42]. Two x-ray tubes and two detectors were arranged orthogonally around a vertical rotating small animal cradle. The animals were scanned while free breathing under anesthesia using 2–3% isoflurane delivered by nose-cone. A pneumatic pillow positioned on the animals' thorax connected to a pressure transducer was used to monitor breathing, and body temperature was maintained with heat lamps, a rectal probe, and a feedback controller. The scanning parameters for the dual-energy scans were: 80 kVp, 160 mA, 10 ms/exposure for the first imaging chain and 40 kVp, 250 mA, 16 ms/exposure for the second imaging chain. Projections from the two imaging chains were acquired simultaneously at each angle of rotation. A total of 360 views were acquired for each chain over a full 360° rotation.

**Table 1.** Radiation therapy imaging study experimental treatment groups.

| | 0 Gy | 5 Gy | 10 Gy | 20 Gy |
|---|---|---|---|---|
| No AuNPs | n = 6 | n = 5 | n = 5 | n = 6 |
| PEG-AuNPs | - | n = 5 | n = 7 | n = 6 |
| RGD-AuNPs | - | n = 7 | n = 8 | - |

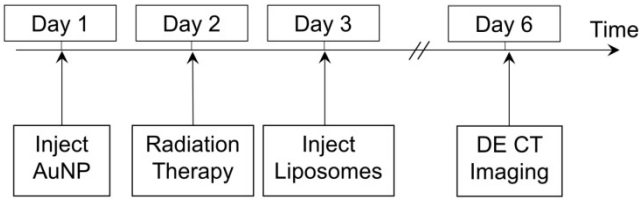


**Figure 1. Imaging protocol timeline.** RT occurred 24 hours after gold nanoparticle injection, which was followed 24 hours later by injection of liposomal iodine. Dual-energy CT imaging was performed 3 days after iodine injection to allow sufficient time for iodine accumulation in the tumors.

## Dual-Energy CT Post Processing

Dual-energy material decomposition was used to generate 3D concentration maps of gold and iodine within each of the CT scans. Raw 40 kVp and 80 kVp datasets were reconstructed using the Feldkamp algorithm [43] in the Cobra EXXIM software package (EXXIM Computing, Livermore, CA). The images were reconstructed in a 512×512×512 matrix with 88 µm isotropic voxel size. Affine registration was performed to improve registration between corresponding 40 and 80 kVp reconstructed volumes using ANTs, an open-source, ITK-based registration toolkit [44, 45]. To improve the results of the dual-energy decomposition, each data set was de-noised using joint bilateral filtration, as described previously [46, 47]. Dual-energy decomposition of gold and iodine was performed after registration and filtration, using the corresponding 80 and 40 kVp filtered data by solving the following linear system at each voxel:

$$x = A^{-1}b$$

Expanding the linear system:

$$\begin{bmatrix} C_I \\ C_{Au} \end{bmatrix} = \begin{bmatrix} CT_{I,40} & CT_{Au,40} \\ CT_{I,80} & CT_{Au,80} \end{bmatrix}^{-1} \begin{bmatrix} CT_{40} \\ CT_{80} \end{bmatrix}$$

In this formulation, $x$ is the least-squares solution for the concentration of the iodine ($C_I$) and gold ($C_{Au}$) in mg/mL in the voxel under consideration. $A$ is a constant sensitivity matrix measured in Hounsfield units per contrast agent concentration (HU/mg/mL) for iodine ($CT_{I,40}$, $CT_{I,80}$) and gold ($CT_{Au,40}$, $CT_{Au,80}$) at 40 and 80 kVp, respectively. Finally, $b$ is the intensity of the voxel under consideration at 40 kVp ($CT_{40}$) and 80 kVp ($CT_{80}$) in Hounsfield units. After solution of the

matrix equation in Matlab, voxels with negative concentrations of both materials were set to zero. Voxels with a negative concentration of one material and a positive concentration of the other material were projected onto the subspace of positive concentration for the single material.

Values for the coefficients of the sensitivity matrix at each energy ($CT_{I,40}$, $CT_{I,80}$, $CT_{Au,40}$, and $CT_{Au,80}$) were determined empirically using a calibration phantom as described previously [48]. For the phantom calibration, the CT attenuation of vials containing known gold and iodine concentrations were measured at 40 and 80 kVp, and the coefficients for the sensitivity matrix were determined by fitting the known gold and iodine concentrations to the measured CT attenuation using a linear least squares regression at each energy level. The derived values for $CT_{I,40}$, $CT_{I,80}$, $CT_{Au,40}$, and $CT_{Au,80}$ used in this study were 28.7, 42.6, 88.5, and 58.8 HU/mg/mL, respectively. In vitro and in vivo validation of the accuracy of this decomposition method has been shown in our previous work [48, 49]. These validation studies demonstrated the ability of this decomposition method to accurately measure gold and iodine concentrations both in vitro and in vivo.

## CT Image Analysis

CT images of the tumors were manually segmented in Avizo (Version 8.1, Visualization Sciences Group, FEI, Hillsboro, OR) using the iodine concentration map from the dual-energy decomposition. Rough regions were manually drawn outside the borders of the tumors, and those regions were thresholded to select only the voxels that contained an iodine concentration greater than 2 mg iodine/mL. This threshold value was chosen to exclude normal tissues and poorly vascularized portions of the tumor (which had no iodine accumulation). The average iodine concentration in each segmented tumor was then measured (after subtracting the background signal of 2 mg iodine/mL) and compared. Gold concentrations within each tumor were also measured following the same method.

For the biodistribution study, gold concentrations within the blood were measured by finding the average gold concentration within multiple (>10) ROIs manually drawn in Avizo within the lumen of the left ventricle, aorta, and inferior vena cava. Other organs (liver and spleen) were manually segmented in Avizo and the average gold concentration within the entire organ was calculated.

## Tumor Darkfield Microscopy

Tumors from each mouse were collected and flash frozen in cryo-embedding medium. Frozen tissue sections (8 µm thickness) were immunostained for the endothelial cell marker CD31. Prior to staining, sections were fixed in 4% paraformaldehyde, rinsed with PBS, and blocked with 10% donkey serum in PBS for one hour. The sections were then incubated with a primary antibody (rat anti-mouse CD31, BD Pharmingen) diluted 1:250 in the blocking buffer for 2 hours at room temperature. The slides were rinsed three times with PBS for 10 minutes, after which the slides were incubated with a secondary antibody (Alexa Fluor488-conjugated donkey anti-rat IgG, Invitrogen) diluted 1:500 in blocking buffer for 1 hour in the dark. Nuclei were counterstained with DAPI.

Immunostained sections were imaged using a Zeiss Axiovert 135 inverted microscope with a Cytoviva darkfield condenser and dual mode fluorescence module fitted with a triple bandpass emission filter. All images were acquired using a 20x lens. Each tumor was imaged using both fluorescence and darkfield modes. Combined darkfield and fluorescence images of each tumor were produced by first thresholding the darkfield images to include only the bright gold nanoparticles. The fluorescence images were then separated into individual color channels in ImageJ (http://imagej.nih.gov/), each of which was thresholded to remove overlapping signals. The resulting images were overlaid with the darkfield image, which allowed visualization of the spatial relationship between the gold nanoparticles and the vasculature and nuclei within the tumors.

## Tumor Combined Radiation and Chemotherapy

The effect of AuNP-augmented RT on tumor delivery of liposomal doxorubicin (Doxil, Janssen) was studied by replacing liposomal iodine in the protocol described above with liposomal doxorubicin. Based on the results of the imaging study, 5 Gy was chosen as the optimal radiation dose for this study, and only RGD-AuNPs were used. 38 mice were randomized into 6 treatment groups: RT + RGD-AuNPs + liposomal doxorubicin (n=5), RT + liposomal doxorubicin (n=7), liposomal doxorubicin alone (n=6), RGD-AuNPs + RT (n=7), RT alone (n=7), and no treatment (n=6). As described above, RGD-AuNPs were injected in mice and the mice were irradiated with 5 Gy 24 hours post injection. A single dose of liposomal doxorubicin was injected into the mice 24 hours after RT. Liposomal doxorubicin was injected at a dose of 4 mg/kg body weight, which is a dose that is well-tolerated in mice and has been shown to slow tumor progression in other mouse tumor models [50]. Tumor size and body weight measurements were collected twice a week after RT

and liposomal doxorubicin injection. Tumor length and width were measured by caliper, and then tumor volume was calculated using the equation $V= (L \times W^2)/2$, where L is the measured tumor length and W is the measured tumor width. Tumor volume doubling time was calculated for each tumor. If the doubling time occurred between measurement time points, the doubling time was calculated by linear interpolation between those time points. The average doubling time for each treatment group was compared to demonstrate growth delay after therapy.

### Statistics

Treatment groups for the iodine accumulation imaging study were split into categories prior to ANOVA and post-hoc testing in order to only perform the relevant pairwise comparisons between treatment groups. One-way ANOVAs were performed for the groups in the 5 Gy treatment level, for the groups in the 10 Gy treatment level, for groups in the 20 Gy treatment level, and for all the control (no AuNP) groups. Following the one-way ANOVA analyses, post-hoc Tukey testing was performed for pairwise comparisons within each of these treatment categories. No pairwise comparisons were performed outside of these treatment categories. Gold accumulation and tumor volume doubling time measurements were each analyzed by a single one-way ANOVA followed by post-hoc Tukey testing for individual comparisons. Error bars in all plots represent the standard error of the mean and statistical significance in all plots is shown at the $p<0.05$ level.

## Results

### Nanoparticle Characterization

TEM images of the bare AuNPs and liposomal iodine are shown in Figure 2A-B. The bare AuNPs have a core diameter of 25 ± 2 nm by TEM. The hydrodynamic diameter and zeta potential measurements (± standard error) for each of the nanoparticles used in this study are shown in Figure 2C. DLS size distributions for the AuNPs and the liposomes are shown in Figure 2D-E. The bare AuNPs increased in size following the addition of PEG, but there is only a small difference in hydrodynamic diameter between the PEG-AuNPs and the RGD-AuNPs. Both liposome formulations have a similar distribution, but the average diameter of the liposomal iodine is slightly higher than the average diameter of the liposomal doxorubicin (118 nm vs. 82 nm) The surface of the citrate-capped AuNPs had a strong negative charge, while surfaces of the PEG-AuNPs, RGD-AuNPs, and liposomes were all near-neutral charge. A neutral surface charge is desirable for in vivo biocompatibility and prolonged circulation time.

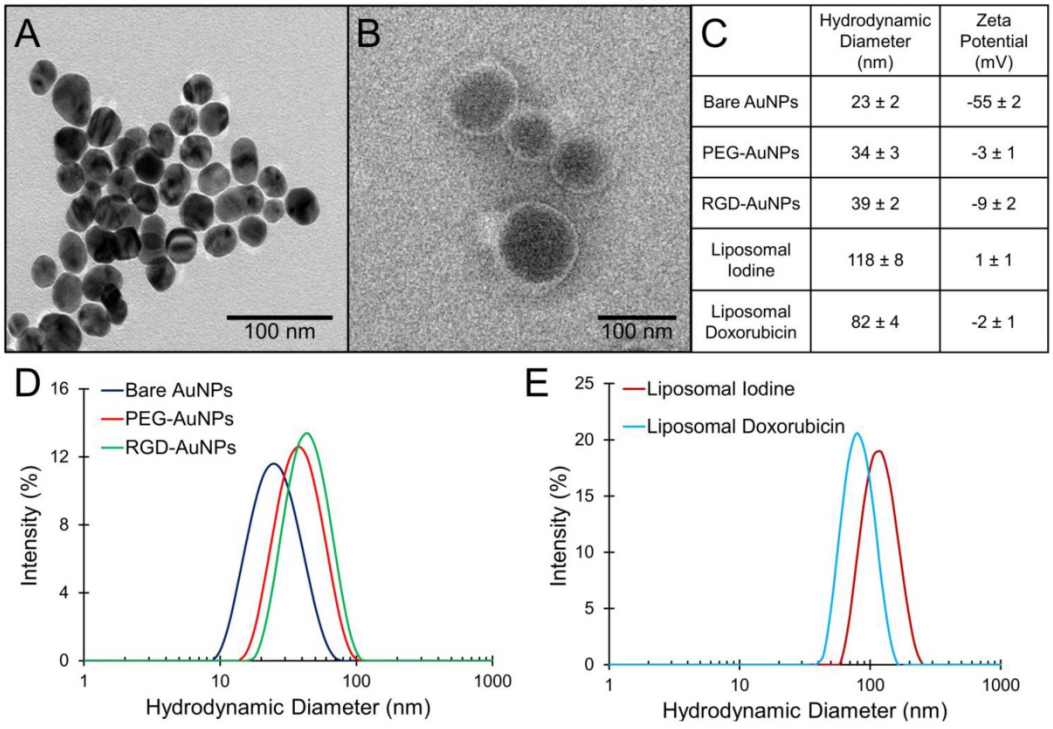


**Figure 2. Characterization of gold nanoparticles and liposomes.** (A) TEM of bare gold nanoparticles, (B) TEM of liposomal iodine, (C) DLS average diameter and zeta potential measurements for each nanoparticle type with the standard error, (D) DLS size distribution of gold nanoparticles, and (E) DLS size distribution of liposomes.

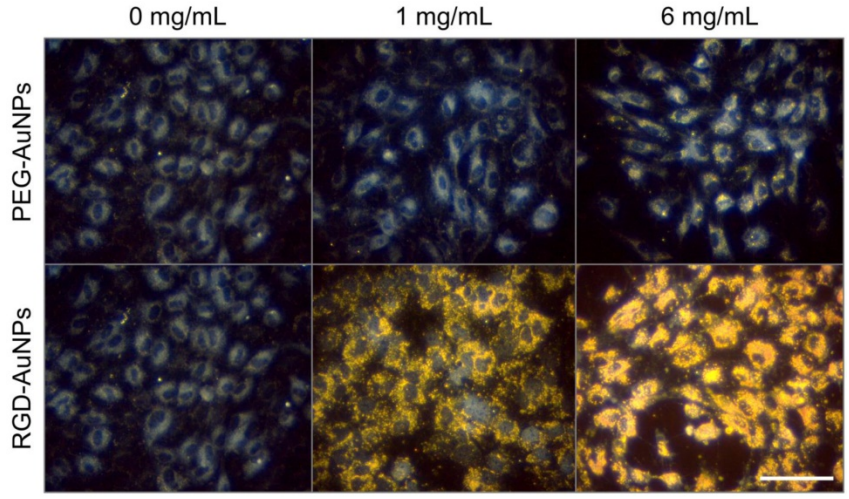


**Figure 3. Darkfield microscopy of endothelial cell targeting by gold nanoparticles.** RGD-AuNPs bind to the endothelial cells to a very high degree at both 1 mg Au/mL and 6 mg Au/mL. PEG-AuNPs show no cell binding at 1 mg Au/mL and only minimal binding at 6 mg Au/mL. The scale bar represents 50 μm and is the same in all panels.

## In Vitro Targeting

The in vitro targeting efficacy of the RGD-AuNPs was tested with HUVECs, which express high levels of the $\alpha_v\beta_3$ integrin [51]. After overnight incubation in cell culture, targeted RGD-AuNPs bound readily to the HUVECs at both low (1 mg Au/mL) and high (6 mg Au/mL) concentrations, while the non-targeted PEG-AuNPs showed no binding at low concentrations and minimal binding at high concentrations. Dark-field images of the gold nanoparticles in culture with HUVECs are shown in Figure 3. At 6 mg Au/mL, the RGD-AuNPs appear to be internalized within the HUVECs, filling the entire cytoplasmic space while sparing the nucleus. RGD-AuNPs are expected to internalize via integrin binding and receptor-mediated endocytosis, which has been well-characterized elsewhere [52-54]. Internalized gold nanoparticles are in close proximity to the cell's nucleus, which increases the likelihood that the extra dose from the gold nanoparticles will damage DNA. For in vivo application, the initial intravascular gold concentration is expected to be >10 mg Au/mL, so this high experimental concentration (6 mg/mL) is within the expected in vivo conditions.

## In Vivo Nanoparticle Biodistribution

The distribution and kinetics of the gold nanoparticles were studied in vivo in a healthy mouse model (C57BL/6). PEG-AuNPs and RGD-AuNPs were injected intravenously and the concentration of gold in the bloodstream was measured over 48 hours. The results are shown in Figure 4A. As expected, the RGD-AuNPs were cleared much more rapidly from the blood relative to the PEG-AuNPs. The estimated blood half-life of the PEG-AuNPs is ~18 hours, while the estimated half-life of the RGD-AuNPs is ~4 hours. The presence of the peptide on the surface of the RGD-AuNPs decreased the nanoparticle circulation time. The RGD-AuNPs had a more negatively charged surface than the PEG-AuNPs, which could allow for more non-specific protein interactions and surface protein adsorption, leading to opsonization and clearance by phagocytes. The peptides themselves also interact with several cell types through the $\alpha_v\beta_3$ integrin receptor. These interactions can further increase the rate of clearance from the blood. At 24 hours after injection, the PEG-AuNPs were at ~45% of their initial concentration, while the RGD-AuNPs decreased to ~2% of their initial concentration in the blood. The concentration of gold within the organs of the reticuloendothelial system (liver and spleen), which typically clear nanoparticles from the blood, was also calculated at the end of the experiment (48 hours). The organ gold concentrations are shown in Figure 4B. The liver and spleen cleared a much higher amount of RGD-AuNPs than PEG-AuNPs at 48 hours after injection, consistent with the rapid clearance from the blood. This suggests that the primary reason for the decreased blood half-life of RGD-AuNPs is increased phagocytosis of the nanoparticles by macrophages within the reticuloendothelial system. Although the bulk concentration of RGD-AuNPs is very low within the blood at 24 hours, the local concentration of gold attached to tumor endothelial cells or internalized within endothelial cells should still be very high (as demonstrated in vitro in Figure 3). With radiation therapy in the tumor imaging study occurring 24 hours after injection, the PEG-AuNPs should be located both within the tumor and within blood vessels, while the RGD-AuNPs should be located almost exclusively either attached to or within the endothelial cells.

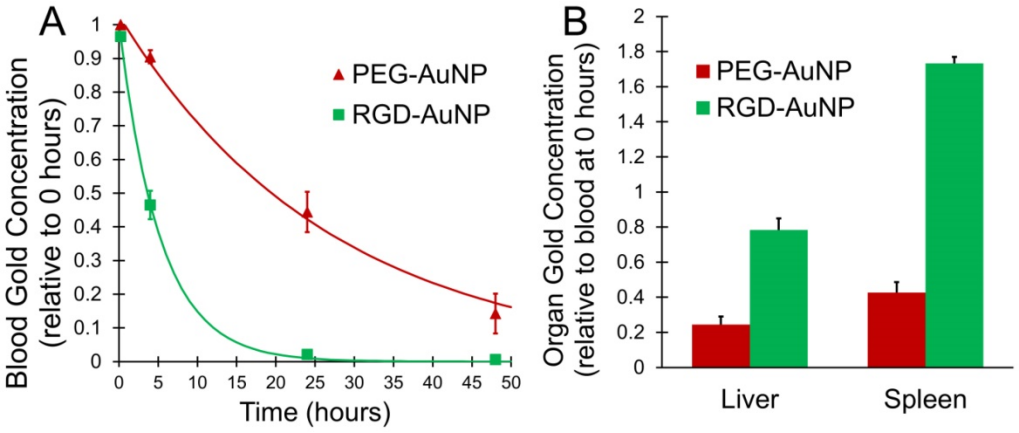


**Figure 4. In vivo gold distribution after IV injection in healthy mice.** (A) Measured concentration for PEG-AuNPs and RGD-AuNPs in the blood over time, along with an exponential fit curve for each nanoparticle type. (B) Organ gold accumulation at 48 hours for each nanoparticle type. The RGD-AuNPs showed more rapid clearance from the blood than PEG-AuNPs as well as increased accumulation in the liver and spleen at 48 hours.

## Tumor Vascular Permeability Imaging

The accumulation of liposomal iodine in tumors after RT (a measure of tumor vascular permeability and a surrogate for liposomal drug delivery) was quantified by dual-energy CT imaging. Using dual-energy CT allowed us to decompose each image into gold and iodine concentration maps, which were then used to quantify the accumulation of iodine in the tumors even when gold nanoparticles were also present. Representative CT images of mice in each treatment group are shown in Figure 5, with the iodine map superimposed on the single-energy grayscale image. Quantification of iodine accumulation in the enhancing regions of each tumor is shown in Figure 6.

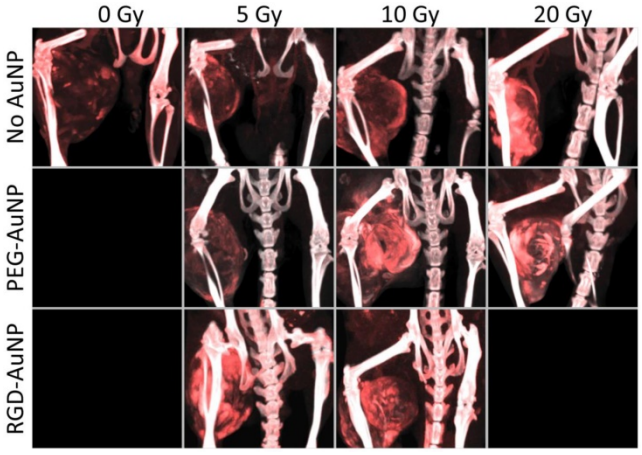


**Figure 5. Maximum intensity projections of the dual-energy CT iodine map for hindlimb sarcomas in each RT treatment group.** Dual-energy CT was performed 3 days after liposomal iodine injection (5 days after gold nanoparticle injection). The iodine map is overlaid on the grayscale 80 kVp dataset. Iodine (red) is present in all the tumors, but is visibly lowest in the no AuNP (0 Gy, 5 Gy, and 10 Gy) groups as well as the PEG-AuNP 5 Gy group. All the other tumors appear to have increased tumor liposomal iodine accumulation as a result of RT. The iodine map is windowed from 2-35 mg iodine/mL. The grayscale images (80 kVp dataset) are windowed from -100-3500 HU.

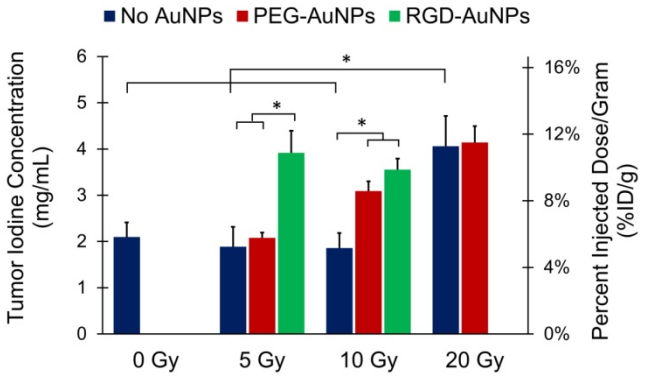


**Figure 6. Tumor liposomal iodine accumulation after gold nanoparticle-augmented radiation therapy.** Concentrations are expressed in both mg iodine/mL (primary axis) and %ID/g (secondary axis). The addition of non-targeted PEG-AuNPs increased the iodine accumulation in the 10 Gy group, but made no change at the 5 Gy or 20 Gy doses. The addition of vascular-targeted RGD-AuNPs led to a large increase in accumulation at 5 Gy (compared to both control and PEG-AuNP groups). At 10 Gy, the addition of RGD-AuNPs did not statistically increase the iodine accumulation compared to PEG-AuNPs, but RGD-AuNPs did increase iodine accumulation compared to the control group with no AuNPs. * represents a statistically significant difference between groups ($p<0.05$).

The first step of our analysis was to determine the dose response of tumor vascular permeability to RT in the absence of AuNPs. We found that the 0 Gy, 5 Gy, and 10 Gy groups (no AuNPs) all had roughly equivalent levels of iodine accumulation (~2 mg iodine/mL after background subtraction, ~5% ID/g), whereas the 20 Gy group had significantly increased iodine accumulation (4.1 mg iodine/mL, 11.3% ID/g). These data suggest that in this sarcoma model there is a threshold for the vascular permeability response to a single dose of RT alone somewhere between 10 and 20 Gy. Below this threshold, no significant increase in permeability was observed, but above this threshold, there was a large increase in vascular permeability.

Next, we studied the effect of adding gold nanoparticles (non-targeted PEG-AuNPs) 24 hours prior to RT at each of these radiation doses. From the initial in vivo kinetics study, we found that these gold

nanoparticles have a blood half-life of ~18 hours (see Figure 4). 24 hours after injection there should be slightly less than 1/2 the original intravascular concentration remaining within the blood vessels as well as significant accumulation of nanoparticles within the tumors (primarily in the perivascular space), so the vasculature is expected to receive a significantly increased radiation dose because of secondary electrons from the AuNPs. Indeed, the 10 Gy PEG-AuNP group had significantly higher iodine accumulation than the 10 Gy control group, demonstrating effective vascular disruption at this dose with AuNP-augmentation. However, at 5 Gy the addition of PEG-AuNPs did not lead to increased vascular permeability. Furthermore, at 20 Gy we also observed no improvement in vascular permeability as a result of AuNP-augmentation, which suggests that 20 Gy by itself is sufficient to cause a near maximal increase in vascular permeability. Although this hypothesis could be tested by treating sarcomas with even higher radiation doses to further explore the dose-response for vascular permeability, in this study we focused on maximizing vascular permeability with AuNP at relatively low radiation doses as an approach to limit radiation-induced toxicity.

Because we hypothesized that vascular-targeted gold nanoparticles would increase the delivered dose of radiation to endothelial cells more than non-targeted nanoparticles, we repeated the low dose (5 Gy and 10 Gy) experiments with RGD-AuNPs. Our goal was to test whether the targeted nanoparticles with RT could have a greater effect on the tumor vasculature at lower radiation doses than was seen with non-targeted AuNPs or RT alone. At 5 Gy, there was a large and statistically significant increase in iodine accumulation in the RGD-AuNP group (3.9 mg iodine/mL, 10.9% ID/g) compared to both the PEG-AuNP group and control group (~2 mg iodine/mL for both, ~5% ID/g). This level of iodine accumulation was similar to what was observed in the 20 Gy treatment groups with and without PEG-AuNPs, which suggests that there was a very large dose enhancement delivered to the endothelium with vascular-targeted AuNPs. When the sarcomas were treated with 10 Gy, we also observed a large increase in iodine accumulation for the RGD-AuNP group compared to 10 Gy alone. The RGD-AuNPs increased the iodine accumulation a small amount relative to PEG-AuNPs, but the difference was not statistically significant. In the CT images in Figure 5, the PEG-AuNP tumor actually appears brighter than the RGD-AuNP tumor; however, this visual difference is primarily due to a higher gold concentration in the PEG-AuNP tumor (which increases the brightness of the grayscale image) as discussed in the following paragraph. Although RGD-AuNPs improved radiation delivery to the endothelium at both 5 and 10 Gy, the effect of RGD-AuNPs relative to non-targeted PEG-AuNPs was greater at 5 Gy.

Gold nanoparticle accumulation in each tumor was also measured to determine what effects radiation dose and nanoparticle type had on overall gold accumulation. The gold nanoparticles were injected 24 hours prior to RT, which gave them time to start to accumulate in the tumor due to EPR. Some of the nanoparticles remained in the blood after RT, so they could continue to accumulate in the tumors after the vascular permeability had increased. Therefore, we hypothesized that tumor gold accumulation would correlate with tumor iodine accumulation. Representative CT images of mice in each treatment group are shown in Figure 7, with the gold map superimposed on the single-energy (80 kVp) grayscale image. Quantification of gold accumulation within the enhancing regions of each tumor is shown in Figure 8. Gold accumulation in the PEG-AuNP groups agrees well with iodine accumulation in those same groups. 5 Gy with PEG-AuNP showed low levels of gold accumulation, while gold concentrations increased in the 10 Gy group and peaked in the 20 Gy groups. Both RGD-AuNP groups, on the other hand, showed very low accumulation of gold nanoparticles five days after injection. This is most likely due to the decreased blood residence time of the RGD-AuNPs relative to PEG-AuNPs, which gives less time for tumor accumulation to occur. It is also possible that targeting the AuNPs to endothelial cells limited the penetration of nanoparticles into the tumor tissue.

Examination of the dual-energy CT gold maps after RT also revealed the presence of gold nanoparticles within the intestinal wall in the RGD-AuNP group, but not in the PEG-AuNP group. CT images of intestinal enhancement in mice 2 days and 5 days after RGD-AuNP injection are shown in Figure S1. Enhancement appears to decrease from 2 days to 5 days, but the intestines remained enhanced 5 days after gold injection.

## Tumor Darkfield Microscopy

Following the CT imaging study, frozen sections of the tumors were imaged using combined immunofluorescence and darkfield microscopy. Sections were stained for endothelial cells (CD31, green) and nuclei (DAPI, blue). Overlays of the immunofluorescence images with the gold nanoparticles visualized by darkfield microscopy are shown in Figure 9. Tumors show a significant amount of gold accumulation for both the PEG-AuNP and

RGD-AuNP groups. The tumors were harvested five days after gold nanoparticle injection, which gave the gold nanoparticles sufficient time to diffuse away from the vasculature and throughout the tumor tissue. This is well-demonstrated in the PEG-AuNP group (Figure 9A), which has gold nanoparticles spread out fairly uniformly over the whole field-of-view. The RGD-AuNP group (Figure 9B), on the other hand, has an uneven distribution of nanoparticles, with many nanoparticles clustering together in several regions and only a small number of nanoparticles spread through the rest of the field-of-view. In some areas, it appears that a large collection of gold nanoparticles is located intracellularly (see white arrows in Figure 9B). Because the RGD-AuNPs are targeted to endothelial cell receptors, this uneven distribution of nanoparticles after accumulation in a tumor is expected.

## Tumor Combined Radiation and Chemotherapy

Following the successful demonstration of increased liposomal iodine accumulation with 5 Gy RT augmented with RGD-AuNPs, we next tested whether RGD-AuNP augmentation of the effect of RT on tumor vascular permeability could increase the delivery and effectiveness of liposomal doxorubicin under the same conditions. Consistent with the imaging protocol, mice were injected with RGD-AuNPs 24 hours prior to RT (5 Gy) and were injected with liposomal doxorubicin 24 hours after RT. Six different treatment groups were used with different combinations of RT, liposomal doxorubicin, and RGD-AuNPs. Tumor growth delay after treatment was tracked by monitoring tumor size over time. Tumor doubling time was calculated for each treatment group, as shown in Figure 10. Tumors in the control group (no treatment) doubled in size on average after ~2 days, while the RT only, RGD-AuNP + RT, liposomal doxorubicin only, and RT + liposomal doxorubicin groups had tumor doubling times of 3-4 days (not statistically different than controls). The group receiving RGD-AuNP-augmented RT together with liposomal doxorubicin had a significantly higher tumor volume doubling time (~8 days) compared to all other treatment groups. From these results, it is clear that 5 Gy RT alone (with or without RGD-AuNPs) was not sufficient to have a significant treatment effect. Although the imaging study showed vascular disruption with 5 Gy RT combined with RGD-AuNPs, this vascular disruption alone was not enough to cause significant tumor growth delay. Likewise, liposomal doxorubicin alone was not sufficient to have a significant treatment effect. Even when combined with 5 Gy RT (no AuNPs), liposomal doxorubicin had little effect on tumor growth rate. This is consistent with the results of our imaging study, which showed that 5 Gy RT alone does not lead to vascular disruption and increased liposome delivery. The addition of RGD-AuNPs together with 5 Gy RT and liposomal doxorubicin significantly improved the treatment effect compared to RT (no AuNPs) + liposomal doxorubicin, suggesting that the presence of AuNPs enhanced vascular disruption and increased the delivery of liposomal doxorubicin into the tumor, consistent with the previous results.

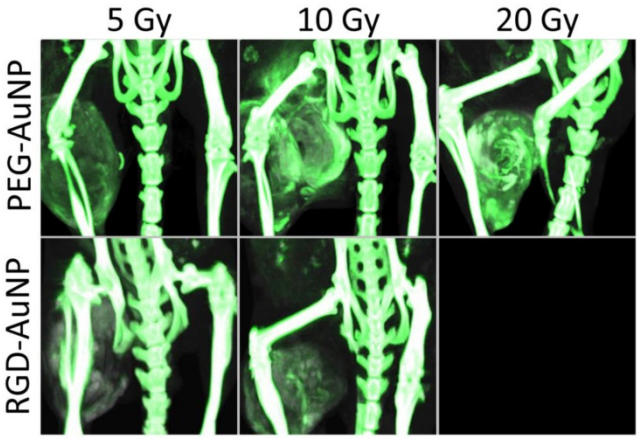


**Figure 7. Maximum intensity projections of the dual-energy CT gold map for hindlimb tumors in each AuNP-RT treatment group.** Dual-energy CT was performed 3 days after liposomal iodine injection (5 days after gold injection). Gold nanoparticle accumulation (shown in green) appears to be the highest in the PEG-AuNP groups that also had higher iodine accumulation (10 Gy and 20 Gy). Gold accumulation in the PEG-AuNP 5 Gy group is visibly lower than the other PEG-AuNP groups. Both RGD-AuNP groups show very low gold accumulation in the tumors, despite the increased vascular permeability seen in these groups in the iodine imaging. The gold map (green) is windowed between 2.5 mg Au/mL and 40 mg Au/mL. The grayscale images (80 kVp dataset) are windowed from -100 HU to 3500 HU.

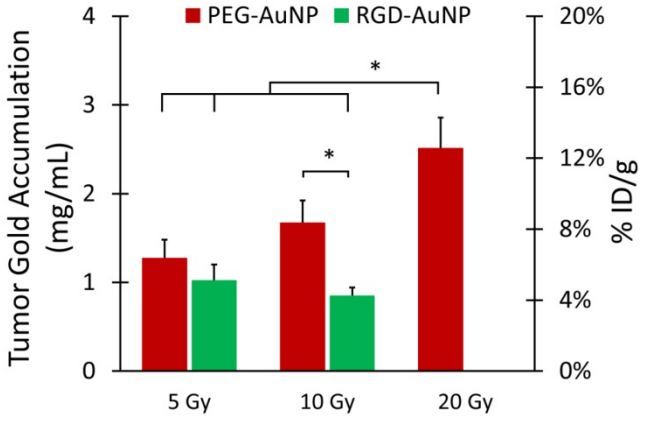


**Figure 8. Tumor gold accumulation after gold nanoparticle-augmented radiation therapy.** Concentrations are expressed in both mg Au/mL (primary axis) and %ID/g (secondary axis). Gold accumulation was quantified by dual-energy CT 3 days after liposomal iodine injection (5 days after gold injection). The highest gold accumulation was seen in the PEG-AuNP 10 Gy and 20 Gy groups, which also demonstrated high vascular permeability to liposomal iodine. The lowest gold accumulation was seen in the RGD-AuNP groups, despite the increased vascular permeability to liposomal iodine seen in these groups. Accumulation in the 20 Gy group was significantly higher than that of all the other groups except 10 Gy PEG-AuNP. The accumulation in the 10 Gy PEG-AuNP group was significantly higher than that of the 10 Gy RGD-AuNP group. * represents a statistically significant difference between groups ($p<0.05$).

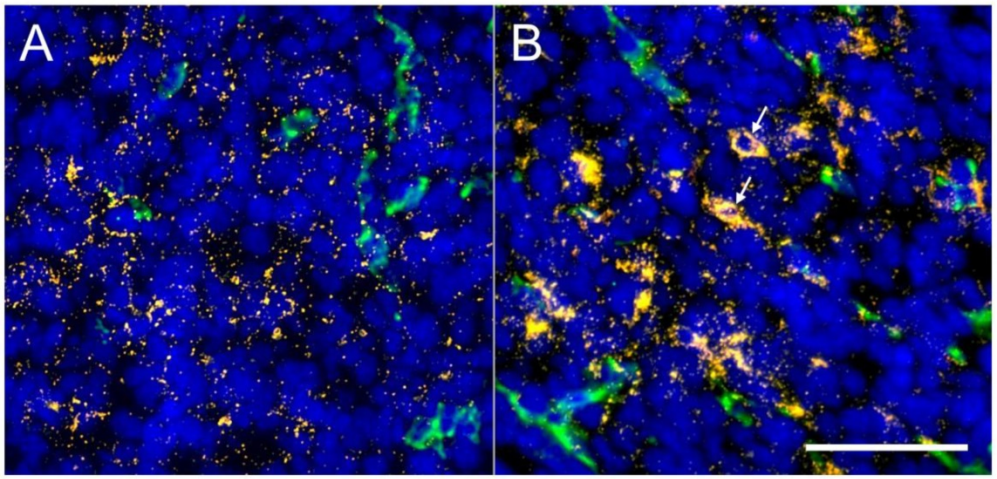


**Figure 9. Darkfield and immunofluorescence microscopy of tumor sections.** Endothelial cells are shown in green (CD31), cell nuclei are shown in blue (DAPI) and gold nanoparticles are shown in orange. (A) Tumor section from a mouse injected with PEG-AuNPs. (B) Tumor section from a mouse injected with RGD-AuNPs. Nanoparticles are readily visualized in both groups, but the overall distribution differs. The PEG-AuNPs are spread throughout the tissue relatively uniformly, while the RGD-AuNPs are grouped together in smaller regions. In some cases, the nanoparticles appear to be located intracellularly (white arrows). The scale bar represents 50 μm and is the same in both panels.

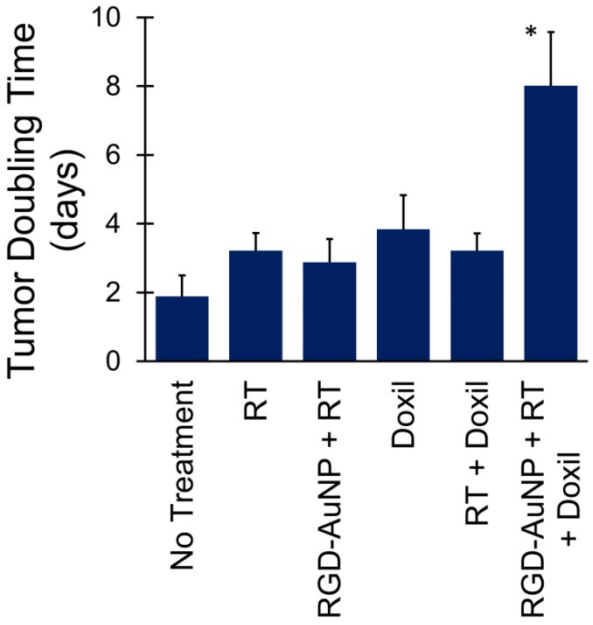


**Figure 10. Tumor volume doubling time for mice treated with RT and liposomal doxorubicin.** The combined therapy with vascular-targeted RGD-AuNPs, RT, and liposomal doxorubicin showed a significant growth delay (higher doubling time) compared to all other treatment groups. The other treatment groups showed a small increase in tumor doubling time compared to the non-treated control mice, but these differences were not statistically significant.

## Discussion and Conclusions

These results show that RT can increase the permeability of tumor vasculature to liposomal iodine and that the increase in permeability is dependent on radiation dose. This increased liposomal iodine delivery can be translated to the delivery of liposomal drugs. Our previous work studying vascular disruption following RT [34] showed that a high dose of RT (20 Gy) caused a significant increase in vascular permeability within the sarcoma tumor model. In this study, we aimed to use AuNPs to augment the radiation dose to endothelial cells in order to reduce the dose of RT necessary for vascular disruption. With the addition of gold nanoparticles, the radiation dose required to increase tumor vascular permeability decreased significantly, particularly for vascular-targeted AuNPs. After treatment with 5 Gy (with RGD-AuNPs), the tumor vascular permeability was equivalent to the vascular permeability after treatment with 20 Gy in the absence of AuNPs. This low dose of RT combined with targeted AuNPs was sufficient to cause the full biological effect seen with much higher doses of RT. These results are consistent with microscopic analysis performed in previous studies [29], which showed endothelial cell and basement membrane disruption as well as significant changes in vascular morphology following low-dose (10 Gy) irradiation with vascular-targeted AuNPs.

Although tumor iodine accumulation increased significantly following targeted-AuNP with RT, the accumulation of gold nanoparticles was actually lower in this targeted group. There are several possible reasons for the low accumulation of targeted-AuNP in the tumors, despite the high accumulation of iodine in the same mice. First, the RGD-AuNPs have a shorter blood half-life than the PEG-AuNPs due to the presence of peptide on the surface of the nanoparticles and slightly more negative charge on the nanoparticle surface. Once vascular disruption occurred, there were more nanoparticles left in the bloodstream in mice injected with the PEG-AuNPs than with the RGD-AuNPs, so more PEG-AuNPs accumulated than RGD-AuNPs. Second, the RGD-AuNPs may not accumulate in the tumors as much due to their endothelial cell binding and internalization. When the targeted AuNPs pass

through the tumor blood vessels, they bind strongly to the endothelial cells, which may prevent them from passing out of the bloodstream into the tumor tissue. In this case, although the concentration of AuNPs on the surface of the endothelium would be high, the concentration of AuNPs within the tumor would be very low. This effect has been seen with high-affinity tumor-targeted antibodies, which show decreased distribution through a tumor with higher receptor binding affinity [55]. A similar effect has also been seen with blood-brain barrier targeting, where antibodies with very high affinity for the transferrin receptor remain stably attached to the blood-brain barrier even after transcytosis, so they do not distribute into the brain. Lower affinity antibodies, on the other hand, can be released from the blood-brain barrier and travel into the brain [56].

Figure S1 shows intestinal enhancement after RGD-AuNP injection. Intestinal targeting is not usually reported in studies using RGD as a targeting ligand, but the effect has been previously described [57]. This study determined the biodistribution of RGD-targeted proteins and found significantly increased small intestine accumulation for RGD-targeted groups compared to controls. On histological analysis, they found that the RGD-targeted proteins were located entirely within the vasculature of the small intestines, showing that the RGD peptides were binding to the intestinal blood vessels, but not penetrating into the intestinal tissue [57]. Gold nanoparticles also accumulate over time within the reticuloendothelial system of the liver and spleen (see Figure 4B). The presence of gold nanoparticles in normal organs, including the liver, spleen, and small intestine could be problematic for treating tumors near those organs with RT because the radiation dose enhancement from the presence of AuNPs would also occur in those tissues, thereby increasing off-target radiation damage. In this study, the hind-limb sarcomas were far from the liver, spleen, and intestines, so no off-target dose enhancement would be expected, but this is an important consideration in radiotherapy treatment planning with AuNPs for tumors that might be in close proximity to these abdominal organs.

Accumulation and long-term retention of gold nanoparticles in the body is a potential concern for clinical applications. There is strong evidence supporting the biocompatibility and non-toxicity of gold nanoparticles [14, 58, 59], but each formulation is unique and must be individually tested for long-term toxicity. Some gold nanoparticle products are in clinical trials, including gold nanoparticle-based tumor necrosis factor (CYT-6091, CytImmune Inc.), which is a tumor vascular disrupting agent, and gold nanoshells (AuroLase, Nanospectra Inc.), which are used for tumor photothermal therapy. Although long-term safety in humans has not yet been conclusively proven, the trials currently support the safe use of gold nanoparticles in humans for therapeutic purposes [60-62].

The accumulation of liposomal iodine in this imaging study represents a surrogate for the amount of liposomal drug that could be delivered to tumors under those same conditions. The effectiveness of liposomal chemotherapeutic agents is dependent on their ability to accumulate specifically in tumors due to high tumor vascular permeability. In this study, we showed that the combination of vascular-targeted AuNPs with relatively low-dose RT (5 Gy) increased the effectiveness of liposomal doxorubicin therapy in primary mouse soft tissue sarcomas, as predicted by the results of the imaging study. In the absence of RT, liposomal doxorubicin injection modestly increased tumor doubling time, but this was not statistically significant. This suggests that some liposomal doxorubicin perfuses into the tumors due to natural tumor vascular leakiness. Adding 5 Gy RT (with no AuNPs) to liposomal doxorubicin administration did not improve the treatment effect. This is consistent with the imaging results, which showed that 5 Gy RT (with no AuNPs) was not sufficient to increase tumor vascular permeability. However, when vascular-targeted AuNPs and 5 Gy RT were administered prior to liposomal doxorubicin administration, a significant increase in tumor growth delay was observed. This is consistent with the imaging data, which showed a large increase in tumor vascular permeability with targeted AuNPs and 5 Gy RT.

One of the limitations of translating nanoparticle-based chemotherapeutics into the clinic is the inconsistency of the EPR effect in humans compared to mouse models [33]. Whereas most mouse tumor models exhibit substantial nanoparticle accumulation due to EPR, human trials are much more varied. Therefore, many liposomal drugs that have shown great promise in animal models have had limited success when translated to patients [33, 63]. Liposomal chemotherapeutic formulations have the potential for greatly improving cancer therapy by increasing the dose delivered to the tumor while reducing the systemic dose and the associated side effects. However, liposomal drugs are not effective if the tumors do not have high inherent vascular permeability. The use of AuNP-augmented RT prior to treatment with liposomal chemotherapeutics could greatly improve liposome delivery to the tumors by disrupting the tumor vasculature and increasing its permeability to nanoparticles. Several other methods of improving liposome delivery to tumors have been

studied, including augmenting vascular permeability factors (bradykinin, nitric oxide, prostaglandins) in tumors [7, 64], inducing hypertension pharmacologically [63, 65], treating the tumor with hyperthermia [66], and damaging the vasculature with photothermal heating [67] or RT without AuNP augmentation [34, 68, 69]. In this study, we have shown that the external beam radiation dose necessary to increase vascular permeability can be decreased substantially by augmenting the radiation delivery to the vasculature with the injection of vascular-targeted AuNPs. By combining AuNPs that target blood vessels with RT focused on a tumor, the extra radiation dose delivered by the AuNPs can be deposited predominantly in vessels within the tumor rather than in surrounding tissues. Therefore, the combination therapy can disrupt the vasculature specifically in tumors to increase the delivery of liposomal chemotherapeutics to tumors while minimizing normal tissue toxicity and thereby widen the therapeutic window.

The methods shown in this study also demonstrate the effectiveness of using CT imaging with liposomal contrast agents to measure the EPR effect. This can potentially be translated to patients, where tumors with high vascular permeability can be identified with CT imaging of liposomal contrast agents prior to making the choice of whether or not to use a liposomal chemotherapeutic agent. This could enable precision medicine, where only the tumors with high inherent vascular permeability would be treated with liposomal agents. Similarly, CT imaging to assess EPR could also be useful for selecting patients for intraoperative molecular imaging with fluorescent imaging agents that accumulate in tumors at least in part through EPR effects [70]. Imaging of EPR in large animal models can be accomplished with radio-labelled liposomes [71] or with nanoparticle-based contrast agents for MRI or fluorescence imaging [33]. However, using CT to measure vascular permeability in tumors could have major advantages because CT is routinely used in the clinic for anatomical tumor imaging and CT is the main imaging modality used in conjunction with RT for tumor delineation and treatment planning. The dual-energy CT material decomposition method used in this study has been well-characterized and validated in our previous work [48, 49]. Dual-energy CT is used extensively in clinical imaging, so these protocols could readily be modified for use in a clinical setting. The development of clinical spectral CT scanners with photon-counting detectors is expected to further improve our ability to resolve multiple materials. Accurate material decomposition of gold and iodine in rabbits using a modified clinical CT scanner and photon-counting detectors has recently been described [72]. As this technology develops, the applications for material decomposition in clinical CT imaging will continue to grow.

One of the limitations for clinical translation of this study is that RT was performed using kilovoltage x-rays, while most modern clinical RT is done with megavoltage x-rays in order to increase the depth of x-ray energy deposition. The interaction cross-section of gold nanoparticles for megavoltage x-rays is significantly lower than the interaction cross-section for kilovoltage x-rays because of the decreasing contribution of the photoelectric effect at high photon energies. Because both gold and water primarily absorb megavoltage x-rays through Compton scattering, their mass attenuation coefficients are nearly identical at 1 MeV. However, a gold nanoparticle is almost 20 times denser than water, so a gold nanoparticle will absorb even megavoltage x-rays much more effectively than water and will therefore produce a region of significant dose enhancement in the immediate environment. Additionally, as megavoltage x-rays pass through tissue, there is significant beam softening, as scattering events lead to the production of many lower energy (kilovoltage) photons and secondary electrons. Up to 20% of the photons are in the low energy (<150 keV) range at a depth of 10 cm in tissue during megavoltage irradiation [6]. Because gold nanoparticles are very effective at absorbing these lower energy photons and electrons, this beam softening significantly increases the effectiveness of gold nanoparticles in megavoltage therapy. Many studies incorporating gold nanoparticles with megavoltage irradiation have shown effective dose enhancement and therapeutic benefit [6, 26, 73, 74], particularly when the gold nanoparticles are actively targeted to cells [21, 28, 75, 76]. Although this study did not employ megavoltage x-rays, the overall impact of AuNP-augmented radiation therapy on tumor vasculature and liposome delivery should be similar for clinical megavoltage applications.

In conclusion, our theranostics approach based on dual-energy CT imaging and RT augmented with vascular-targeted AuNPs has the potential to significantly improve the selective delivery of liposomal chemotherapies to tumors and thereby increase the efficacy and reduce the side effects from both RT and chemotherapy.

## Abbreviations

AuNP: gold nanoparticle; CT: x-ray computed tomography; RGD: (Arg-Gly-Asp) peptide; RT: radiation therapy; EPR: enhanced permeability and retention; PEG: polyethylene glycol; TEM:

transmission electron microscopy; DLS: dynamic light scattering; PBS: phosphate-buffered saline.

## Acknowledgments

This imaging study was performed at the Duke Center for In Vivo Microscopy, an NIH/NIBIB national Biomedical Technology Resource Center (P41 EB015897). This research was supported by a grant from Susan G. Komen for the Cure® (IIR13263571) and by NIH funding through the National Cancer Institute (R01 CA196667, U24 CA220245, R35 CA197616). Jeffrey Ashton was supported by an NIH/NIBIB F30 Fellowship (5 F30 EB020512). We would like to thank Jocelyn Hoye for her assistance with manual tumor segmentation. We also thank Dr. Yvonne Mowery, Amy Wisdom and Lorraine Da Silva Campos for help with providing animals and performing radiation therapy.

## Supplementary Material

Figure S1. http://www.thno.org/v08p1782s1.pdf

## Competing Interests

David Kirsch is on the scientific advisory board of Lumicell Inc, which is a company commercializing intraoperative imaging and is a co-founder of XRAD Therapeutics, which is developing radiosensitizers. The other authors have declared that no competing financial interest exists.

## References

1. Yi A, Kim HH, Shin HJ, Huh MO, Ahn SD, Seo BK. Radiation-induced complications after breast cancer radiation therapy: a pictorial review of multimodality imaging findings. Korean J Radiol. 2009; 10: 496-507.
2. Haubner F, Ohmann E, Pohl F, Strutz J, Gassner HG. Wound healing after radiation therapy: review of the literature. Radiat Oncol. 2012; 7: 162.
3. Bentzen SM. Preventing or reducing late side effects of radiation therapy: radiobiology meets molecular pathology. Nat Rev Cancer. 2006; 6: 702-13.
4. Moding EJ, Kastan MB, Kirsch DG. Strategies for optimizing the response of cancer and normal tissues to radiation. Nat Rev Drug Discov. 2013; 12: 526-42.
5. Hainfeld JF, Dilmanian FA, Slatkin DN, Smilowitz HM. Radiotherapy enhancement with gold nanoparticles. J Pharm Pharmacol. 2008; 60: 977-85.
6. Schuemann J, Berbeco R, Chithrani DB, Cho SH, Kumar R, McMahon SJ, et al. Roadmap to Clinical Use of Gold Nanoparticles for Radiation Sensitization. Int J Radiat Oncol Biol Phys. 2016; 94: 189-205.
7. Maeda H, Nakamura H, Fang J. The EPR effect for macromolecular drug delivery to solid tumors: Improvement of tumor uptake, lowering of systemic toxicity, and distinct tumor imaging in vivo. Adv Drug Deliv Rev. 2013; 65: 71-9.
8. Maeda H, Wu J, Sawa T, Matsumura Y, Hori K. Tumor vascular permeability and the EPR effect in macromolecular therapeutics: a review. J Control Release. 2000; 65: 271-84.
9. Cai QY, Kim SH, Choi KS, Kim SY, Byun SJ, Kim KW, et al. Colloidal gold nanoparticles as a blood-pool contrast agent for X-ray computed tomography in mice. Invest Radiol. 2007; 42: 797-806.
10. Ahn S, Jung SY, Lee SJ. Gold Nanoparticle Contrast Agents in Advanced X-ray Imaging Technologies. Molecules. 2013; 18: 5858-90.
11. Alivov Y, Baturin P, Le HQ, Ducote J, Molloi S. Optimization of K-edge imaging for vulnerable plaques using gold nanoparticles and energy resolved photon counting detectors: a simulation study. Phys Med Biol. 2014; 59: 135-52.
12. Anton N, Vandamme TF. Nanotechnology for Computed Tomography: A Real Potential Recently Disclosed. Pharm Res. 2014; 31: 20-34.
13. Au JT, Craig G, Longo V, Zanzonico P, Mason M, Fong Y, et al. Gold nanoparticles provide bright long-lasting vascular contrast for CT imaging. AJR Am J of Roentgenol. 2013; 200: 1347-51.
14. Hainfeld JF, Slatkin DN, Focella TM, Smilowitz HM. Gold nanoparticles: a new X-ray contrast agent. Br J Radiol. 2006; 79: 248-53.
15. Hainfeld JF, Lin L, Slatkin DN, Avraham Dilmanian F, Vadas TM, Smilowitz HM. Gold nanoparticle hyperthermia reduces radiotherapy dose. Nanomedicine. 2014; 10: 1609-17.
16. Jeremic B, Aguerri AR, Filipovic N. Radiosensitization by gold nanoparticles. Clin Transl Oncol. 2013; 15: 593-601.
17. Hainfeld JF, Smilowitz HM, O'Connor MJ, Dilmanian FA, Slatkin DN. Gold nanoparticle imaging and radiotherapy of brain tumors in mice. Nanomedicine. 2013; 8: 1601-9.
18. Hainfeld JF, Dilmanian FA, Zhong Z, Slatkin DN, Kalef-Ezra JA, Smilowitz HM. Gold nanoparticles enhance the radiation therapy of a murine squamous cell carcinoma. Phys Med Biol. 2010; 55: 3045-59.
19. Hainfeld JF, Slatkin DN, Smilowitz HM. The use of gold nanoparticles to enhance radiotherapy in mice. Phys Med Biol. 2004; 49: N309-N15.
20. Park J, Park J, Ju EJ, Park SS, Choi J, Lee JH, et al. Multifunctional hollow gold nanoparticles designed for triple combination therapy and CT imaging. J Control Release. 2015; 207: 77-85.
21. Wolfe T, Chatterjee D, Lee J, Grant JD, Bhattarai S, Tailor R, et al. Targeted gold nanoparticles enhance sensitization of prostate tumors to megavoltage radiation therapy in vivo. Nanomedicine. 2015; 11: 1277-83.
22. Martinov MP, Thomson RM. Heterogeneous multiscale Monte Carlo simulations for gold nanoparticle radiosensitization. Med Phys. 2017; 44: 644-53.
23. Rosa S, Connolly C, Schettino G, Butterworth KT, Prise KM. Biological mechanisms of gold nanoparticle radiosensitization. Cancer Nanotechnol. 2017; 8: 2.
24. Ferrero V, Visona G, Dalmasso F, Gobbato A, Cerello P, Strigari L, et al. Targeted dose enhancement in radiotherapy for breast cancer using gold nanoparticles, part 1: A radiobiological model study. Med Phys. 2017; 44: 1983-92.
25. Hwang C, Kim JM, Kim J. Influence of concentration, nanoparticle size, beam energy, and material on dose enhancement in radiation therapy. J Radiat Res. 2017; 58: 1-7.
26. Retif P, Pinel S, Toussaint M, Frochot C, Chouikrat R, Bastogne T, et al. Nanoparticles for Radiation Therapy Enhancement: the Key Parameters. Theranostics. 2015; 5: 1030-44.
27. Miao L, Huang L. Exploring the tumor microenvironment with nanoparticles. Cancer Treat Res. 2015; 166: 193-226.
28. Lin Y, Paganetti H, McMahon SJ, Schuemann J. Gold nanoparticle induced vasculature damage in radiotherapy: Comparing protons, megavoltage photons, and kilovoltage photons. Med Phys. 2015; 42: 5890-902.
29. Kunjachan S, Detappe A, Kumar R, Ireland T, Cameron L, Biancur DE, et al. Nanoparticle Mediated Tumor Vascular Disruption: A Novel Strategy in Radiation Therapy. Nano Lett. 2015; 15: 7488-96.
30. Danhier F, Le Breton A, Preat V. RGD-based strategies to target alpha(v) beta(3) integrin in cancer therapy and diagnosis. Mol Pharm. 2012; 9: 2961-73.
31. Kunjachan S, Pola R, Gremse F, Theek B, Ehling J, Moeckel D, et al. Passive versus Active Tumor Targeting Using RGD- and NGR-Modified Polymeric Nanomedicines. Nano Lett. 2014; 14: 972-81.
32. Mout R, Moyano DF, Rana S, Rotello VM. Surface functionalization of nanoparticles for nanomedicine. Chem Soc Rev. 2012; 41: 2539-44.
33. Prabhakar U, Maeda H, Jain RK, Sevick-Muraca EM, Zamboni W, Farokhzad OC, et al. Challenges and key considerations of the enhanced permeability and retention effect for nanomedicine drug delivery in oncology. Cancer Res. 2013; 73: 2412-7.
34. Moding EJ, Clark DP, Qi Y, Li Y, Ma Y, Ghaghada K, et al. Dual-energy micro-computed tomography imaging of radiation-induced vascular changes in primary mouse sarcomas. Int J Radiat Oncol Biol Phys. 2013; 85: 1353-9.
35. Lee CL, Min H, Befera N, Clark D, Qi Y, Das S, et al. Assessing cardiac injury in mice with dual energy-microCT, 4D-microCT, and microSPECT imaging after partial heart irradiation. Int J Radiat Oncol Biol Phys. 2014; 88: 686-93.
36. Frens G. Controlled Nucleation for Regulation of Particle-Size in Monodisperse Gold Suspensions. Nat Phys Sci. 1973; 241: 20-2.
37. Mukundan Jr S, Ghaghada KB, Badea CT, Kao CY, Hedlund LW, Provenzale JM, et al. A liposomal nanoscale contrast agent for preclinical CT in mice. AJR Am J Roentgenol. 2006; 186: 300.
38. Jain PK, Lee KS, El-Sayed IH, El-Sayed MA. Calculated absorption and scattering properties of gold nanoparticles of different size, shape, and composition: applications in biological imaging and biomedicine. J Phys Chem B. 2006; 110: 7238-48.
39. Kirsch DG, Dinulescu DM, Miller JB, Grimm J, Santiago PM, Young NP, et al. A spatially and temporally restricted mouse model of soft tissue sarcoma. Nat Med. 2007; 13: 992-7.
40. Moding EJ, Castle KD, Perez BA, Oh P, Min HD, Norris H, et al. Tumor cells, but not endothelial cells, mediate eradication of primary sarcomas by stereotactic body radiation therapy. Sci Transl Med. 2015; 7: 278ra34.
41. Moding EJ, Lee CL, Castle KD, Oh P, Mao L, Zha S, et al. Atm deletion with dual recombinase technology preferentially radiosensitizes tumor endothelium. J Clin Invest. 2014; 124: 3325-38.
42. Badea C, Johnston S, Johnson B, De Lin M, Hedlund LW, Johnson GA. A Dual Micro-CT System for Small Animal Imaging. Proc SPIE. 2008; 6913: 691342.
43. Feldkamp LA, Davis LC, Kress JW. Practical cone-beam algorithm. J Opt Soc Am. 1984; 1: 612-19.
44. Avants BB, Tustison NJ, Song G, Cook PA, Klein A, Gee JC. A reproducible evaluation of ANTs similarity metric performance in brain image registration. Neuroimage. 2011; 54: 2033-44.

45. Hermosillo G, Chefd'Hotel C, Faugeras O. Variational methods for multimodal image matching. Int J Comput Vision. 2002; 50: 329-43.
46. Badea CT, Guo X, Clark D, Johnston SM, Marshall CD, Piantadosi CA. Dual-energy micro-CT of the rodent lung. Am J Physiol Lung Cell Mol Physiol. 2012; 302: L1088-97.
47. Clark D, Johnson GA, Badea CT. Denoising of 4D Cardiac Micro-CT Data Using Median-Centric Bilateral Filtration. Proc SPIE. 2012; 8314: 83143Z.
48. Clark D, Ghaghada K, Moding E, Kirsch D, Badea C. In vivo characterization of tumor vasculature using iodine and gold nanoparticles and dual energy micro-CT. Phys Med Biol. 2013; 58: 1683-704.
49. Ashton JR, Clark DP, Moding EJ, Ghaghada K, Kirsch DG, West JL, et al. Dual-energy micro-CT functional imaging of primary lung cancer in mice using gold and iodine nanoparticle contrast agents: a validation study. PLoS One. 2014; 9: e88129.
50. Rios-Doria J, Durham N, Wetzel L, Rothstein R, Chesebrough J, Holoweckyj N, et al. Doxil synergizes with cancer immunotherapies to enhance antitumor responses in syngeneic mouse models. Neoplasia. 2015; 17: 661-70.
51. Albert JM, Cao C, Geng L, Leavitt L, Hallahan DE, Lu B. Integrin alpha v beta 3 antagonist Cilengitide enhances efficacy of radiotherapy in endothelial cell and non-small-cell lung cancer models. Int J Radiat Oncol Biol Phys. 2006; 65: 1536-43.
52. Wu PH, Onodera Y, Ichikawa Y, Rankin EB, Giaccia AJ, Watanabe Y, et al. Targeting integrins with RGD-conjugated gold nanoparticles in radiotherapy decreases the invasive activity of breast cancer cells. Int J Nanomedicine. 2017; 12: 5069-85.
53. Moncelet D, Bouchaud V, Mellet P, Ribot E, Miraux S, Franconi JM, et al. Cellular density effect on RGD ligand internalization in glioblastoma for MRI application. PLoS One. 2013; 8: e82777.
54. Lin RY, Dayananda K, Chen TJ, Chen CY, Liu GC, Lin KL, et al. Targeted RGD nanoparticles for highly sensitive in vivo integrin receptor imaging. Contrast Media Mol Imaging. 2012; 7: 7-18.
55. Adams GP, Schier R, McCall AM, Simmons HH, Horak EM, Alpaugh RK, et al. High affinity restricts the localization and tumor penetration of single-chain fv antibody molecules. Cancer Res. 2001; 61: 4750-5.
56. Yu YJ, Zhang Y, Kenrick M, Hoyte K, Luk W, Lu Y, et al. Boosting brain uptake of a therapeutic antibody by reducing its affinity for a transcytosis target. Sci Transl Med. 2011; 3: 84ra44.
57. Schraa AJ, Kok RJ, Moorlag HE, Bos EJ, Proost JH, Meijer DK, et al. Targeting of RGD-modified proteins to tumor vasculature: a pharmacokinetic and cellular distribution study. Int J Cancer. 2002; 102: 469-75.
58. Cervenka L, Mitchell KD, Navar LG. Renal function in mice: effects of volume expansion and angiotensin II. J Am Soc Nephrol. 1999; 10: 2631-6.
59. Lin MD, Marshall CT, Qi Y, Badea C, Piantadosi C, Johnson GA. Quantitative blood flow measurements in the small animal cardiopulmonary system using digital subtraction angiography. Med Phys. 2009; 36: 5347-58.
60. Gad SC, Sharp KL, Montgomery C, Payne JD, Goodrich GP. Evaluation of the toxicity of intravenous delivery of Auroshell particles (Gold-silica nanoshells). Int J Toxicol. 2012; 31: 584-94.
61. Libutti SK, Paciotti GF, Byrnes AA, Alexander HR, Jr., Gannon WE, Walker M, et al. Phase I and pharmacokinetic studies of CYT-6091, a novel PEGylated colloidal gold-rhTNF nanomedicine. Clin Cancer Res. 2010; 16: 6139-49.
62. Stern JM, Kibanov Solomonov VV, Sazykina E, Schwartz JA, Gad SC, Goodrich GP. Initial Evaluation of the Safety of Nanoshell-Directed Photothermal Therapy in the Treatment of Prostate Disease. Int J Toxicol. 2016; 35: 38-46.
63. Maeda H. Vascular permeability in cancer and infection as related to macromolecular drug delivery, with emphasis on the EPR effect for tumor-selective drug targeting. Proc Jpn Acad Ser B Phys Biol Sci. 2012; 88: 53-71.
64. Seki T, Fang J, Maeda H. Enhanced delivery of macromolecular antitumor drugs to tumors by nitroglycerin application. Cancer Sci. 2009; 100: 2426-30.
65. Noguchi A, Takahashi T, Yamaguchi T, Kitamura K, Noguchi A, Tsurumi H, et al. Enhanced tumor localization of monoclonal antibody by treatment with kininase II inhibitor and angiotensin II. Jpn J Cancer Res. 1992; 83: 240-3.
66. Kong G, Braun RD, Dewhirst MW. Characterization of the effect of hyperthermia on nanoparticle extravasation from tumor vasculature. Cancer Res. 2001; 61: 3027-32.
67. Melancon MP, Elliott AM, Shetty A, Huang Q, Stafford RJ, Li C. Near-infrared light modulated photothermal effect increases vascular perfusion and enhances polymeric drug delivery. J Controlled Release. 2011; 156: 265-72.
68. Appelbe OK, Zhang Q, Pelizzari CA, Weichselbaum RR, Kron SJ. Image-Guided Radiotherapy Targets Macromolecules through Altering the Tumor Microenvironment. Mol Pharm. 2016; 13: 3457-67.
69. Davies Cde L, Lundstrom LM, Frengen J, Eikenes L, Bruland SO, Kaalhus O, et al. Radiation improves the distribution and uptake of liposomal doxorubicin (caelyx) in human osteosarcoma xenografts. Cancer Res. 2004; 64: 547-53.
70. Whitley MJ, Cardona DM, Lazarides AL, Spasojevic I, Ferrer JM, Cahill J, et al. A mouse-human phase 1 co-clinical trial of a protease-activated fluorescent probe for imaging cancer. Sci Transl Med. 2016; 8: 320ra4.
71. Hansen AE, Petersen AL, Henriksen JR, Boerresen B, Rasmussen P, Elema DR, et al. Positron Emission Tomography Based Elucidation of the Enhanced Permeability and Retention Effect in Dogs with Cancer Using Copper-64 Liposomes. ACS Nano. 2015; 9: 6985-95.
72. Cormode DP, Si-Mohamed S, Bar-Ness D, Sigovan M, Naha PC, Balegamire J, et al. Multicolor spectral photon-counting computed tomography: in vivo dual contrast imaging with a high count rate scanner. Sci Rep. 2017; 7: 4784.
73. Tsiamas P, Liu B, Cifter F, Ngwa WF, Berbeco RI, Kappas C, et al. Impact of beam quality on megavoltage radiotherapy treatment techniques utilizing gold nanoparticles for dose enhancement. Phys Med Biol. 2013; 58: 451-64.
74. Saberi A, Shahbazi-Gahrouei D, Abbasian M, Fesharaki M, Baharlouei A, Arab-Bafrani Z. Gold nanoparticles in combination with megavoltage radiation energy increased radiosensitization and apoptosis in colon cancer HT-29 cells. Int J Radiat Biol. 2017; 93: 315-23.
75. McMahon SJ, Hyland WB, Muir MF, Coulter JA, Jain S, Butterworth KT, et al. Nanodosimetric effects of gold nanoparticles in megavoltage radiation therapy. Radiother Oncol. 2011; 100: 412-6.
76. Zhao N, Yang Z, Li B, Meng J, Shi Z, Li P, et al. RGD-conjugated mesoporous silica-encapsulated gold nanorods enhance the sensitization of triple-negative breast cancer to megavoltage radiation therapy. Int J Nanomedicine. 2016; 11: 5595-610.